Longevity-Oriented and Reliable Forwarding Percolation Routing in Underwater Acoustic Sensor Networks

Yuan Liu, *Member, IEEE*, Haiyan Wang, Lin Cai, *Fellow, IEEE*, Junhao Hu, and Xiaohong Shen, *Member, IEEE*

***Abstract*—In underwater acoustic sensor networks (UANs), reliable packet delivery is critical in data collection and monitoring of the oceans. It primarily relies on the design of routing protocols to guarantee network durability and connectivity. However, utilizing routing design to achieve enhanced network longevity and reliable packet forwarding is challenging due to the complex underwater environment, unstable link connectivity, high transmission power, and high propagation latency. Thus, we propose a novel routing strategy called the longevity-oriented and reliable forwarding percolation (LRP) routing protocol. The goal of LRP is to ensure reliability by exploring multipath percolation-based routing and extend network longevity by energy control and residual energy optimization. Network reliability can be estimated using a built-in calculation model, and the source node controls energy and records the residual energy to extend the network lifetime. Utilizing an optimization of the network reliability requirement and residual energy, we develop a routing strategy to select the activated link set and node set for each hop in an energy-saving and reliable way. Moreover, a recursive approach is used to avoid the occurrence of void regions. Simulation results exhibit the effectiveness of the power control and routing strategy and demonstrate its superiority over the benchmarks in terms of network longevity and reliability.**

***Index Terms*—Energy efficiency, network longevity, routing protocol design, underwater acoustic sensor network (UAN), underwater communication.**

I. Introduction

THE EARTH'S oceans, covering approximately 70% of the planet's surface, harbor abundant marine biomass energy, valuable seabed mineral reserves, and unexplored marine territory. Consequently, the exploration, comprehension, and sustainable utilization of the ocean have become focal points of research, aiming to support a wide range of intelligent ocean applications [1], such as underwater artificial intelligence, underwater big data analytics, and autonomous underwater systems. These applications mainly involve reliable data delivery and long-term monitoring of selected ocean areas [2]. Energy-efficient and reliable routing protocols are essential to prolong the network longevity for ocean monitoring missions and improve end-to-end (ETE) reliability. Our research primarily centers on horizontal packet forwarding among sensor nodes deployed on the ocean floor, distinct from vertical forwarding. The focus on horizontal transmission arises from its well-known challenges attributed to multipath propagation, rendering it more complex than vertical channels, demonstrating comparatively higher distortion characteristics [3]. The underwater acoustic sensor networks (UANs) considered in this article are multihop and anchored on the sea floor: each sensor node can conduct sensing, transmission, and relaying tasks. All data packets are routed to an undersea sensor node closest to the sink node. The considered submarine network system model has crucial characteristics, shown in Section III-A.

However, underwater acoustic channels have unique attributes, which introduce various challenges in designing routing strategies for enhanced network connectivity and longevity. The underwater acoustic channel exhibits a stark contrast to the terrestrial wireless channel. First, limited spectrum, frequency-dependent attenuation, multipath propagation, and low speed of sound (approximately 1500 m/s) contribute to the most challenging communication media [4]. Second, it is worth noting that power consumption in UANs is heavily influenced by the transmission range and modulation techniques employed. In the receive mode, the power consumption usually falls within the range of 0.1–1 W, contingent upon the complexity of the receiver. During a continuous transmission mode, the power consumption tends to be higher, typically ranging from 10 to 100 W. Given the limited energy supply and high cost to replace or recharge underwater sensor nodes, when a node depletes its energy, it ceases to function, and the associated links become disabled. The overall longevity of the network is compromised when dead nodes lead to network disconnection. Thus, the residual energy needs to be considered

Manuscript received 26 July 2023; revised 4 October 2023; accepted 26 October 2023. Date of publication 3 November 2023; date of current version 7 March 2024. This work was supported in part by the Key Program of the National Natural Science Foundation of China under Grant 62031021; in part by the National Natural Science Foundation of China under Grant 62071385; and in part by the China Scholarship Council under Grant 202006290193. *(Corresponding author: Haiyan Wang.)*

Yuan Liu and Xiaohong Shen are with the School of Marine Science and Technology and the Key Laboratory of Ocean Acoustics and Sensing, Ministry of Industry and Information Technology, Northwestern Polytechnical University, Xi'an 710072, Shaanxi, China (e-mail: yuan_l@mail.nwpu.edu.cn; xhshen@nwpu.edu.cn).

Haiyan Wang is with the School of Marine Science and Technology and the Key Laboratory of Ocean Acoustics and Sensing, Ministry of Industry and Information Technology, Northwestern Polytechnical University, Xi'an 710072, Shaanxi, China, and also with the School of Electronic Information and Artificial Intelligence, Shaanxi University of Science and Technology, Xi'an 710021, Shaanxi, China (e-mail: hywang@sust.edu.cn).

Lin Cai and Junhao Hu are with the Department of Electrical and Computer Engineering, University of Victoria, Victoria, BC V8W 3P6, Canada (e-mail: cai@ece.uvic.ca).

Digital Object Identifier 10.1109/JIOT.2023.3329715

during routing design. Third, links may be erratic and intermittently connected due to unpredictable water movement and node impairments. Additionally, void regions may arise when a relay node cannot find forwarders within its transmission range, potentially leading to communication gaps and data forwarding issues.

On the one hand, to address the above issues, UANs cannot directly apply the existing strategies on long-lifetime and reliable routing in traditional terrestrial networks. For example, frequent exchange of control messages to maintain routing tables may be prohibitively costly in UANs due to high transmission power and long propagation delay. On the other hand, previous studies on UANs have primarily focused on opportunistic and geographical routing protocols for vertical networks. It is also worth paying more attention to the design of the routing protocol for data collection in horizontal UANs.

This article proposes a longevity-oriented and reliable forwarding routing (LRP) strategy motivated by the percolation theory to address link fragility and network lifetime in UANs. LRP starts with the construction of a hop-based graph, where it optimizes the allocation of transmission power and retransmission times to nodes through energy control. This optimization aims to conserve energy while ensuring reliable link success probability. The source node estimates the reliability of each hop to obtain a suitable candidate link set and candidate node set. These sets can be further trimmed using a residual energy constraint, which balances the energy cost of nodes for different forwarding periods. The proposed protocol aims to maximize network longevity without sacrificing network connectivity, achieved by utilizing concurrent multipath transmissions to guarantee ETE reliability and energy control to balance energy costs. Moreover, the source node uses a recursive algorithm to recover the void region problem. The main contributions of this article are as follows.

1) An analytical framework quantifying the underwater link success probability and ETE reliability is developed based on the grid network.
2) We design an energy control scheme in the initialization phase to save energy consumption during packet forwarding. Based on the topology characteristics and the analytical framework, a link selection algorithm is developed that uses the estimated reliability and the remaining energy of candidate nodes.
3) We design a novel longevity-oriented and reliable forwarding percolation routing protocol named LRP that forwards packets in a percolation manner along the activated links selected. Simulation results show that for UANs LRP routing strategy guarantees reliable data delivery and achieves a superior network longevity performance compared to the benchmarks.

The remainder of this article is organized as follows. Section II is related work. Section III introduces the system model, underwater acoustic link propagation model, and ETE reliability calculation model. We describe in detail the operations of LRP in Section IV. In Section V, we conduct an analysis and optimize the parameters. Section VI is dedicated to showing and discussing the simulation results. Finally, Section VII is the conclusion of this article.

II. Related Work

Using grid topology with multihop relaying has garnered significant attention in many research studies for underwater data relay and collection, as it allows for long-distance information transmission and broad topology coverage. Raina and Jha [5] analyzed the quality of service of four different square-grid topologies with different sensor orientations. The results showed that the orientations and functionalities of the sensors can be varied to enhance the network throughput, latency, and longevity. Lmai et al. [6] explored a multiline grid network where multiple simultaneous transmissions are allowed using propagation delay. They defined an optimal transmission schedule for all nodes. The upper bound on network throughput was calculated considering the fair access criterion. Wang et al. [7] formulated a multiobjective integer linear programming based on a designed transmission power model for TDMA scheduling in the grid network.

In multihop UANs, the traditional routing scheme establishes a unicast path for packet relay, thereby escalating energy consumption, ETE delay, and channel competition [8]. Thus, multipath opportunistic routing (OR) [9], [10], [11] and energy-efficient routing have garnered significant attention from researchers.

Random underwater acoustic on–off links cause low connectivity and prolonged packet forwarding latency, the OR strategy was proposed to address these issues. Geography location information or distance vector is used in the design of OR. Noh et al. [10] proposed an anycast routing scheme based on pressure sensors focusing on vertical forwarding, where packets are forwarded to the surface sinks. Wang et al. [12] proposed a self-adapting routing strategy to select the node closer to the destination as a relay node because of the proposed self-adapting forwarding probability calculation model. The authors exploited the distance vector in [13] to address the void region and long detour problems in UANs. Recently, new techniques have been introduced to enhance the design of OR. Coutinho and Boukerche [14] proposed a stochastic model for studying OR in multimodal UANs. They presented two heuristics algorithms for the next-hop acoustic modem and candidate selection. By different acoustic modems and routing selection to improve energy efficiency and data delivery. In [15], a reinforcement learning-based OR was proposed to select the appropriate relay nodes and address the issue of void regions based on the nodes' comprehensive peripheral status. Although these protocols effectively address the issue of low connectivity, they do not take into account the combined consideration of network reliability and energy consumption.

Furthermore, UANs also encounter the challenge of uneven energy consumption, which reduces network longevity [16], [17]. Energy efficient is critical for UANs routing. In [18], a power-efficient routing was proposed to reduce the unnecessary power consumption imposed by the forwarder node selection phase and forwarding set trimming phase. In [19], reinforcement learning was introduced to achieve a more uniform distribution of residual energy among sensor nodes during the routing process. Draz et al. [20] proposed a routing with the watchman node to address the low packet

delivery ratio and the void hole problem. In [21], a centralized energy-aware routing scheme was proposed to save energy consumption in multimodal UANs. They formulated the routing problem to optimize several long-term global performance metrics. To prolong the network longevity, Zhou et al. [22] proposed any path routing based on Q-learning, using remaining energy and nodes geography information to calculate Q-value that guides the routing selection. Reinforcement learning was incorporated into an adaptive clustering routing protocol in [23] to prolong network longevity. According to the bias reward function, the cluster head is easier to be a relay node, and the cluster head can be changed with the environment information. Liu et al. [24] proposed an energy-efficient routing (EEGNBR) protocol based on a guiding network, using the distance vector and concurrent working data forwarding mechanism to provide an energy-saving and reliable routing for UANs.

However, in the literature, there needs to be more exploration of performance-guaranteed routing based on theoretical analysis for underwater networks with grid topology. During the last decades, percolation theory [25], the mathematical study of percolation, has introduced new understanding and techniques to various fields, including physics and complex networks. The scenario of a liquid flowing through a porous material, traversing from one hole to another and reaching the bottom, can be mathematically represented as a network comprising $n \times n$ vertices, referred to as "site." Each site is connected to its neighboring sites through an edge or "bond." The liquid can pass through these edges when open with a probability of p. Otherwise, these edges are closed with a probability of $1 - p$, independently of other edge states. By determining the probability of an open path from top to bottom for a given p, we can gain insight into the behavior of liquids in porous materials [26]. This probability calculation is the basis for percolation-type routing, which can be used to design routing protocols that provide reliability guarantees in UANs with a grid topology. The percolation process, which is used to model the behavior of liquids in porous materials, can also mimic the message-flooding process in communication networks. This process inspired the percolation routing design investigated in this article.

III. System Model and Reliability Analysis

This section introduces the system model, underwater acoustic link propagation model, and the ETE reliability calculation model used in this work.

A. System Model

Consider an acoustic sensor network consisting of sinks at the oceans' surface and $N = n \times m$ sensor nodes anchored undersea. One of these nodes, denoted by v_s, periodically generates sensing data frames and sends them to seafloor node v_d nearest to a sink at the ocean's surface. Sensor nodes can forward or route packets to node v_d, which may involve multiple nodes in the relay process to reach v_d. In this work, we focus specifically on the routing among nodes on the seafloor. Frames are forwarded directionally hop by hop from v_s to v_d

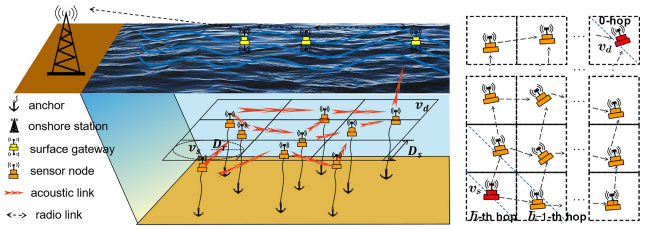

Fig. 1. (a) Network architecture. (b) Grid topology.

to avoid looping, which is based on a directional graph built by the initialization. The process of a frame being forwarded through many different paths mimics the percolation process, so we call this percolation routing.

For convenience, we illustrate the grid deployment of sensor nodes, as shown in Fig. 1(a), where each node is anchored in a square with a side length of D_s. To allow for placement errors, we assume that each node is randomly positioned within a circle at the center of each square unit, with a radius of D_r. Nodes in adjacent squares are connected by acoustic wireless links.

Given the grid topology with directional links, the number of hops to reach a node from v_d can be determined by topology discovery discussed in Section IV-B. We define the set of nodes h hop away from v_d as set V_h and the set of links connecting nodes from V_{h+1} to V_h as set E_h, assuming that v_s is $\hbar$ hop away from v_d. $\hbar$ represents the total hop counts of the network, $h \in [0, \hbar]$. In this context, the ith node in V_h is denoted as v_i^h ($v_i^h \in V_h$) and the jth link in E_h is denoted as e_j^h ($e_j^h \in E_h$). The grid topology shown in Fig. 1(b) can be represented as a graph $G = \{V, E\}$, where $V = V_1 \cup V_2, \ldots, \cup V_\hbar$, $E = E_1 \cup E_2, \ldots, \cup E_\hbar$, and $G = G_1 \cup G_2, \ldots, \cup G_\hbar$. Each node v_i^h (excluding the edge nodes on the rightmost and top sides) is connected up to two links.

In this article, node v_s generates data frames with a constant rate and sends its data to node v_d. The information generated by the source node is referred to as "prior information," e.g., following a Poisson distribution. The number of epochs measures the lifetime of the network, and an epoch consists of D_u packets generated by v_s. The initialization procedure will restart before the beginning of each epoch. After that, the link selection will restart and the results will be distributed to all nodes in G. In each epoch, nodes will use the saved routing table to relay packets until the end of the epoch. We assume that the whole topology of typical networks does not change in an epoch.

For percolation routing, the crucial issue is selecting the links to participate in data forwarding, with the selected percolation paths satisfying the energy constraints and the estimated ETE reliability requirement. To identify candidate nodes and links, we define X^h and L^h as the sets of reachable nodes and links at the hth hop. If we use a binary value to denote whether the link is selected as a candidate or not, the link has two cases, corresponding to "1" or "0." We define L_z^h as a candidate link set for the hth hop, where the jth bit of z represents whether the jth link is selected as a candidate link or not. z is in the range of $[0, 2^{a_h} - 1]$, where a_h represents

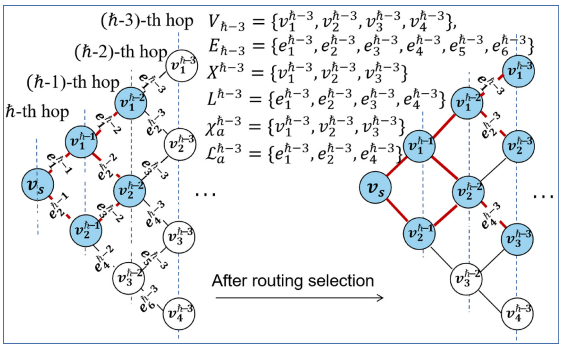

Fig. 2. Illustrative example in which activated links are represented by red lines and activated nodes are denoted by blue circles.

the total number of links that can reach the node in X^h. The node set connected through L_z^h is denoted by X_z^h, namely, the candidate node set.

A link can be activated or deactivated to either allow or prevent its participation in message forwarding. The selected the optimal candidate links and the corresponding nodes are referred to as the activated link set $\mathcal{L}_a$ ($\mathcal{L}_a = \{\mathcal{L}_a^0, \mathcal{L}_a^1, \ldots, \mathcal{L}_a^{\hbar}\}$) and activated node set $\mathcal{X}_a$ ($\mathcal{X}_a = \{\mathcal{X}_a^0, \mathcal{X}_a^1, \ldots, \mathcal{X}_a^{\hbar}\}$). Conversely, the remaining nodes form a deactivated node set. They cannot forward the packet from v_s to their neighbors to conserve energy.

B. Underwater Acoustic Link Propagation Model

In the subsequent sections, we calculate the acoustic link success probability, taking into account its characteristics and assuming frequency-shift keying (FSK) modulation. For any pair of nodes within their communication range, there may be a link between them; the success probability of a packet can be calculated by following the process. In [27], the calculation process of $\mathrm{SNR}(l_i^h, p_t)$ was introduced in detail according to underwater acoustic theory. The bit error ratio can be expressed as

$$p_e\left(l_i^h, p_t\right) = \frac{1}{\left(10^{(\mathrm{SNR}(l_i^h, p_t)/10)}\right)/2 + 2} \tag{1}$$

where l_i^h is the distance of link e_i^h, and p_t is the transmission power. When a node sends a packet with size pck_{size} bits r_n times using link e_i^h, the corresponding success probability is

$$P_s^{i,h}\left(l_i^h, p_t, r_n\right) = \sum_{j=0}^{r_n-1}\left(1-\exp\left(pck_{\text{size}}\ln\left(1-p_e\left(l_i^h, p_t\right)\right)\right)\right)^j \times \exp\left(pck_{\text{size}}\ln\left(1-p_e\left(l_i^h, p_t\right)\right)\right). \tag{2}$$

To clarify the notation used in this article, we provide an illustrative example in Fig. 2. We denote $P_s^{1,\hbar-2}$ as the success probability of link $e_1^{\hbar-2}$ from node $v_1^{\hbar-1}$ to $v_1^{\hbar-2}$ in Fig. 2.

When node v_i^h sends a packet using link e_j^{h-1} if the received power denotes p_r and the data rate denotes R_b, its energy consumption can be represented as

$$En_i^h\left(r_n, p_t, e_j^{h-1}\right) = \frac{(r_n \times p_t + p_r) \times pck_{\text{size}}}{R_b}. \tag{3}$$

We use pck_q to represent the qth packet sent by node v_i^h. We denote the link set in E_{h-1} used to forward data pck_q by node v_i^h as $\epsilon_i^{h-1}|pck_q$. The residual energy after node v_i^h sends pck_q is shown as

$$Er\left(v_i^h, \epsilon_i^{h-1}|pck_q\right) = Er\left(v_i^h, \epsilon_i^{h-1}|pck_{q-1}\right) - \sum_{e_j^{h-1}\in\epsilon_i^{h-1}|pck_q} En_i^h\left(r_n, p_t, e_j^{h-1}\right) \tag{4}$$

where $Er(v_i^h, \epsilon_i^{h-1}|pck_{q-1})$ is the residual energy of node v_i^h after sending the $(q-1)$th packet, and the latter part of the formula is the energy consumption of node v_i^h relaying the qth packet by links $\epsilon_i^{h-1}|pck_q$.

C. ETE Reliability Calculation Model

To elucidate the ETE reliability calculation model, we employ an illustrative example to present the notations, as depicted in Fig. 2. The process is to select links for data from the source node v_s, where the node set $V_{\hbar-3} = \{v_1^{\hbar-3}, v_2^{\hbar-3}, v_3^{\hbar-3}, v_4^{\hbar-3}\}$ are those nodes $(\hbar-3)$th hop away from the destination, and link set $E_{\hbar-3} = \{e_1^{\hbar-3}, e_2^{\hbar-3}, e_3^{\hbar-3}, e_4^{\hbar-3}, e_5^{\hbar-3}, e_6^{\hbar-3}\}$ are the links between nodes in $V_{\hbar-3}$ and $V_{\hbar-2}$. Assuming the activated links of $E_{\hbar}$, $E_{\hbar-1}$ and $E_{\hbar-2}$ are given as shown in Fig. 2, the reachable node set in $V_{\hbar-3}$ is $X^{\hbar-3} = \{v_1^{\hbar-3}, v_2^{\hbar-3}, v_3^{\hbar-3}\}$, and the corresponding reachable link set to choose from $E_{\hbar-3}$ is $L^{\hbar-3}=\{e_1^{\hbar-3}, e_2^{\hbar-3}, e_3^{\hbar-3}, e_4^{\hbar-3}\}$. After link selection that will be described in detail in Section IV, activated node set and link set for the $(\hbar-3)$th hop are $\mathcal{X}_a^{\hbar-3} = \{v_1^{\hbar-3}, v_2^{\hbar-3}, v_3^{\hbar-3}\}$ and $\mathcal{L}_a^{\hbar-3} = \{e_1^{\hbar-3}, e_2^{\hbar-3}, e_4^{\hbar-3}\}$, respectively.

S_k^h is defined as node state k of set X^h, where the ith bit of the binary form of k represents whether the ith node in X^h receives a copy of the message successfully or not. For instance, $S_3^{\hbar-3}$ indicates that $v_1^{\hbar-3}$ and $v_2^{\hbar-3}$ in $X^{\hbar-3}$ can receive a copy of the message, while the remaining nodes fail to receive it.

Considering node states in X^{h+1}, the state transition probability from S_k^{h+1} to $S_{k'}^h$ is denoted as $H_{k,k'}^h$. We use $P(S_{k'}^h)$ to represent the probability of reaching state $S_{k'}^h$. Given $P(S_k^{h+1})$ and the success probability of the jth link in L^h denoted as $P_s^{j,h}$, we can calculate $P(S_{k'}^h)$. For instance, we can obtain the states $S_{k'}^{\hbar-3}$ in Fig. 2 as follows.

For $S_1^{\hbar-2}$, only $v_1^{\hbar-2}$ is connected, we need to consider its outgoing links $e_1^{\hbar-3}$ and $e_2^{\hbar-3}$. If $e_1^{\hbar-3}$ is connected but $e_2^{\hbar-3}$ is not, $S_1^{\hbar-3}$ can be reached from $S_1^{\hbar-2}$. We have $H_{1,1}^{\hbar-3} = P_s^{1,\hbar-3}(1-P_s^{2,\hbar-3})$. For $S_2^{\hbar-2}$, only $v_2^{\hbar-2}$ is connected and it cannot deliver the message to $v_1^{\hbar-3}$. For $S_3^{\hbar-2}$, $v_1^{\hbar-2}$ and $v_2^{\hbar-2}$ both are connected, so $v_1^{\hbar-3}$, $v_2^{\hbar-3}$, and $v_3^{\hbar-3}$ all should be considered. When $e_1^{\hbar-3}$ is connected but others are not. This state can be expressed as $S_1^{\hbar-3}$. We have $H_{3,1}^{\hbar-3} = P_s^{1,\hbar-3}(1-P_s^{2,\hbar-3})(1-P_s^{4,\hbar-3})$. Then, $P(S_1^{\hbar-3})$ is given by

$$P\left(S_1^{\hbar-3}\right) = P\left(S_1^{\hbar-2}\right)\cdot H_{1,1}^{\hbar-3} + P\left(S_3^{\hbar-2}\right)\cdot H_{3,1}^{\hbar-3}. \tag{5}$$

In general, using the Markov Chain model [28], [29], we have

$$P\left(S_{k'}^h\right) = P\left(S_k^{h+1}\right)\times H_{k,k'}^h. \tag{6}$$

Thus, the ETE reliability to any hop can be calculated by (6).

IV. Routing Protocol Design

In this section, we first formulate the selection of routers as an optimization problem. Then, we introduce the LRP protocol, which consists of the initialization, link selection, and packet forwarding procedures. Finally, the MAC used in LRP is discussed in the last section.

The LRP routing protocol utilizes a flexible multipath percolation scheme to optimize energy efficiency and ensure ETE reliability by selecting suitable nodes for data forwarding. The size and composition of the activated node set may vary during different periods to achieve this goal. At each hop, the number of activated nodes ranges from at least two relays, maximizing the network longevity at the cost of reducing ETE reliability, to all of the nodes at this hop, enhancing ETE reliability but increasing energy consumption. By adjusting the activated links according to the current energy consumption of each link, the residual energy after the previous packet, and the estimated reliability, LRP aims to strike a good tradeoff between energy consumption and reliability.

A. Problem Formulation

The source node's selection of relay links significantly influences ETE reliability and lifetime. To address this, we formulate the problem as an optimization of residual energy while maintaining the constraint on ETE reliability. Particularly, energy optimization aims to maximize the minimum remaining energy of nodes over time, ensuring adherence to energy constraints and prolonging network longevity. Meanwhile, only the nodes that satisfy reliability requirements can be selected as candidate nodes. The activated node set $\mathcal{X}_a^h$ and link set $\mathcal{L}_a^h$ of the hth hop are obtained by the optimal link state solution z^* derived from the optimization problem

$$\max \min_{(v_i^h(z))^*} \left\{\left[Er|\left(L_z^h, pck_q\right)\right], \text{for} \quad z = 1, 2, \ldots, 2^{a_h} - 1\right\} \tag{7}$$

$$\text{s.t.} \quad X_z^h \subseteq V_h, L_z^h \subseteq E_h, a_h \geq 2 \tag{7a}$$

$$Er\left(v_i^h(z), \epsilon_i^{h-1}|pck_{q-1}\right) \geq En_i^h|pck_q, v_i^h(z) \in X_z^h \tag{7b}$$

$$P\left(S_k^h\right) \geq \sqrt[h]{Th} \ (h > 0) \tag{7c}$$

$$\Lambda_{v_i^h} \neq -1. \tag{7d}$$

The objective function is formed by $2^{a_h} - 1$ arrays, which corresponds to L_z^h. $v_i^h(z)$ represents a node v_i in a candidate node set X_z^h. In (7), for each array, node $v_i^h(z)$ ($v_i^h(z) \in X_z^h$) with the minimum residual energy is captured. The node $(v_i^h(z))^*$ with the maximum residual energy among these nodes is then obtained. Thus, the optimal z^* can be obtained by $(v_i^h(z))^*$ and its corresponding node and link sets, $X_{z^*}^h$ and $L_{z^*}^h$, are the activated node set and link set, respectively ($\mathcal{X}_a^h = X_{z^*}^h$, $\mathcal{L}_a^h = L_{z^*}^h$). Constraint (7a) defines that set X_z^h and L_z^h are a subset of V_h and E_h, respectively. The length of L^h is no less than 2. Constraint (7b) requires that the remaining energy of node $v_i^h(z)$ be larger than the energy consumption of one transmission. Constraint (7c) is the reliability constraint, where the probability of node state S_k^h that cannot satisfy the reliability requirement will be trimmed. Th is the ETE reliability threshold set by the source node. In (7d), the energy flag, denoted as $\Lambda_{v_i^h}$, is employed to prevent the acquisition of the optimal local solution, which might lead to rapid depletion of energy in specific nodes.

The energy flag of node v_i^h is expressed as

$$\Lambda_{v_i^h} = \begin{cases} -1, & Er\left(v_i^h, \epsilon_i^{h-1}|pck_q\right) \\ & < \beta\left(\frac{1}{a_h}\sum_{j=1}^{a_h} Er\left(v_j^h, \epsilon_i^{h-1}|pck_q\right)\right) \\ -1, & Er\left(v_i^h, \epsilon_i^{h-1}|pck_q\right) < \min \ En_i^h \\ -1, & \Lambda_{\text{child}|v_i^h} = -1 \\ 1, & \text{otherwise} \end{cases} \tag{8}$$

where β is a coefficient less than 1 to prevent the remaining energy from too low. We use child$|v_i^h$ to denote the node in X^{h-1} that is connected to v_i^h, i.e., the child nodes of v_i^h. There are four situations for the value of $\Lambda_{v_i^h}$. In (8), the first case signifies that node v_i^h assigns its flag a value of -1 when its remaining energy is less than a variable that is related to the average remaining energy of all nodes in set X^h. Thus, the residual energy of the node cannot be shallow; otherwise, the node may be banned for this period. If node v_i^h is insufficient to send any packets because its residual energy cannot support a transmission, its flag is marked as -1, as shown in the second case of (8). Each node has an updated energy flag at the beginning of a new period. The third case in (8) illustrates that the flag of node v_i^h is -1 if the $(h-1)$th hop nodes connected to node v_i^h all have a flag of -1. Otherwise, flag $\Lambda_{v_i^h}$ equals 1 in the last row of (8).

B. Initialization

In this study, the sink node periodically broadcasts initialization commands. After receiving the command, node v_d, which is closest to the sink, initiates and executes the topology discovery procedure to gather essential information about the network topology [30].

The initialization phase involves topology discovery and power control. We assume that the network can achieve time synchronization through the exchange of *hello* packet during the topology discovery. This is a technology that has undergone extensive research and development within the domain of UANs, as extensively described in [31], [32], and [33].

The topology discovery helps to identify the neighboring nodes, determine their connectivity, and establish their hop counts. The topology discovery begins with node v_d, which broadcasts *hello* packet to its neighbors. The *hello* packet contains information, such as location, node ID, $hello_{seq}$, residual energy, and hop count. Nodes that receive the *hello* packet save this information and set their hop count to the sender's hop count plus 1 if they satisfy the grid location conditions. They then broadcast the updated *hello* packet hop by hop until node v_s completes this procedure. This procedure results in the formation of a grid topology, as shown in Fig. 1(b). Assuming that the topology remains relatively stable within a period, it

will be updated after the next discovery period. It is worth noting that the hop count increases hop by hop from node v_d to v_s. Messages are forwarded from the source node to the destination in the data message transmission procedure, i.e., from the $\hbar$th hop to the 0th hop. In the routing selection process, we may refer to the hth hop as the next hop for the $(h+1)$th hop.

The energy control includes configuring p_t and the number of retransmission times. To minimize energy consumption on individual links e_j^{h-1}, we formulate an optimization problem in (9). Constraint (9a) represents that the link success probability is lager than a predefined value of P_{req}. We consider the number of transmission attempts r_n, being less than or equal to 3, as specified in (9b). The distance of link e_j^h is larger than the minimum communication distance l_- and less than the maximum communication distance l_+, as defined in (9c). Constraint (9d) represents that the transmission power is not less than the initial value. The power control process is introduced by solving the optimization problem. Our aim is to reduce energy consumption by adjusting transmission power and transmission times to achieve

$$\min \quad En_i^h\left(r_n, p_t, e_j^{h-1}\right) \tag{9}$$

$$\text{s.t.} \quad P_s^{j,h-1}\left(l_j^{h-1}, p_t, r_n\right) \geq P_{\text{req}} \tag{9a}$$

$$r_n \in N_+, r_n \leq 3 \tag{9b}$$

$$l_- \leq l_j^{h-1} \leq l_+ \tag{9c}$$

$$p_t \geq p_0. \tag{9d}$$

To solve the problem, we first determine the value of P_{req} based on the relationship between ETE reliability and $P_s^{j,h-1}$, serving as a baseline for link success probability requirements. Subsequently, we calculate the total transmission power versus distance, given the maximum transmission attempts of one, two, and three, respectively, when $P_s^{j,h-1} \geq P_{\text{req}}$. This allows us to find the combinations of transmission power p_t and transmission attempts r_n for minimizing energy consumption at different distances. Finally, we obtain a set of solutions, as shown in (10). Each solution corresponds to different distance values, offering the lowest energy consumption while meeting the link's success probability requirements.

C. Link Selection

Following the initialization, the source node executes routing link selection[1] using the optimal problem (7), which consists of two subproblems. First, for routing selection, the current nodes need to select the candidate link set for the next hop, which is obtained utilizing the activated link set at the current hop and (7a)–(7d) through Function CandiSelec() in Algorithm 1. Subsequently, based on the obtained candidate link set from function CandiSelec(), the source node further trims the candidate set to obtain the final activated link and node set hop by hop, as presented in Algorithm 2. However, in some cases, it is possible that the source node cannot obtain activated links and nodes for the next-hop, which results in a void region. To address this issue, the recovery Algorithm 3, VoidRec(), is added to Algorithm 2 to adjust the activated link set.

[1]In light of the periodic dynamic network topology in underwater sensor networks, we schedule the initialization to execute after each epoch D_u.

Algorithm 1 Candidate Set Selection

1: **function:** CandiSelec( )
2: DATA:h, $\mathcal{L}_a^{h+1}$, $\mathcal{X}_a^{h+1}$, Λ and $P_s^{j,h}$
3: RESULT:$\mathbb{L}^h$ and $\mathbb{X}^h$
4: calculate X^h and L^h connecting with the nodes in $\mathcal{X}_a^{h+1}$
5: **for all** link e_j^h in L^h **do**
6: **if** $\Lambda_{v_i^h} = -1$ **then**
7: delete node v_i^h from X^h
8: delete the links connecting with node v_i^h from L^h
9: **end if**
10: **end for**
11: update a_h
12: $z = 1$
13: **while** $z < 2^{a_h}$ **do**
14: **if** $P(S_{k'}^h)|L_z^h \geq \sqrt[h]{Th}$ **then**
15: $\mathbb{X}^h \leftarrow X_z^h$, $\mathbb{L}^h \leftarrow L_z^h$
16: **end if**
17: $z = z + 1$
18: **end while**

The function CandiSelec(), as shown in Algorithm 1, is used by v_s to obtain the candidate link sets and node sets for each hop. By following the steps outlined in the algorithm, it is possible to calculate all the candidate node sets $\mathbb{X}^h$ and link sets $\mathbb{L}^h$ for each hop. Specifically, the source node utilizes the stored topology information to calculate the available node set X^h and link set L^h for each hop in line 4. Nodes v_i^h with a flag $\Lambda = -1$ are eliminated from set X^h and their corresponding links are also removed from set L^h in lines 5–10. The updated L^h results in an updated a_h in line 11. With the updated a_h, the source node can calculate $z = [1, 2^{a_h} - 1]$ and set L_z^h. The reliability $P(S_{k'}^h)$ is calculated under candidate set L_z^h. The candidate link and node sets that satisfy both the energy and reliability constraints are added to set $\mathbb{L}^h$ and $\mathbb{X}^h$, while those that cannot satisfy the reliability constraint are eliminated in lines 12–18. By following this process, the function CandiSelec() is responsible for selecting all reliable candidate link set $\mathbb{L}^h$ and node set $\mathbb{X}^h$ for the hth hop.

Algorithm 2 presents the activated link selection procedure where the source node v_s determines the activated link set and node set based on the results in Algorithm 1. The procedure begins by initializing the activated node set $\mathcal{X}_a$, link set $\mathcal{L}_a$, Λ, and *flag* in lines 4–7, indicating that v_s is the activated node of the $\hbar$th hop and $L^{\hbar}$ is added into set $\mathcal{L}_a$. Λ is the empty set. *flag* is a flag that represents that the source node cannot find a path from the source to the destination in lines 8–24. The source node executes the link selection procedure hop by hop, calculating the activated nodes and links. In particular, in line 10, it uses the function CandiSelec() (given in Algorithm 1) to calculate the total candidate link sets $\mathbb{L}^h$ that satisfy the ETE reliability requirement at the hth hop, with the corresponding candidate node sets in set $\mathbb{X}^h$.

Algorithm 2 Activated Link Selection

1: **function:** LinkSelec( )
2: DATA: Er and $P_s^{i,h}$
3: RESULT:$\mathcal{L}_a$, $\mathcal{X}_a$, and Λ
4: $h = \hbar$
5: $\mathcal{X}_a \leftarrow X^{\hbar}$, $\mathcal{L}_a \leftarrow L^{\hbar}$
6: $P(S_1^{\hbar}) = 1$, $\Lambda \leftarrow \emptyset$
7: *flag*=0
8: **while** $h \neq 1$ **do**
9: $h = h - 1$
10: $[\mathbb{X}^h, \mathbb{L}^h]$=CandiSelec( )
11: **while** $\mathbb{X}^h == \emptyset$ **do**
12: $[\mathbb{X}^h, \mathbb{L}^h, h]$=VoidRec( )
13: **if** $h == \hbar - 1$ **then**
14: *flag*=1
15: return
16: **end if**
17: **end while**
18: **if** *flag* $== 0$ **then**
19: max min $\{Er|(L_z^h, pck_q)$, for L_z^h in $\mathbb{L}^h\}$
20: $\mathcal{X}_a^h \leftarrow (X_{z^*}^h)$, $\mathcal{L}_a^h \leftarrow (L_{z^*}^h)$, $P(S_k^h)|X_{z^*}^h$
21: **else**
22: return
23: **end if**
24: **end while**
25: **while** $h \neq \hbar$ **do**
26: update $\Lambda_{v_i^h}$
27: $h = h + 1$
28: **end while**

If $\mathbb{X}^h$ is null, the source node cannot find out any activated link-set, and a void region occurs. The void recovery VoidRec() function in line 12 (detail in Algorithm 3) reselects the activated link-set for the $(h+1)$th hop and the hth hop to repeat the selection procedure in a recursive manner. If the adjusted activated link set is not null after the function of VoidRec(), it can continue to execute the following calculation in lines 18–28; otherwise, if the candidate node set cannot be obtained until $h = \hbar - 1$, the link selection ends in lines 13–16.

When $\mathbb{X}^h$ is not null, i.e., the flag equals 0, line 19, respectively, calculates the node with minimum residual energy in L_z^h and compares the minimum residual energy of nodes from different set to select the one whose minimum residual energy is the maximum. $X_{z^*}^h$ is selected as the optimal set representing the activated node set, and $L_{z^*}^h$ is the optimal link state that corresponds to the activated nodes. Line 20 saves the activated node set, link set, and the reliability of the hth hop and continues to calculate the (h-1)th hop in line 9, and so on. If the flag equals 1, which represents that the source node cannot select a path because nodes have run out of energy. The routing process will be terminated.

When the source node completes the link selection from the $\hbar$th hop to the 0th hop, it updates the flag $\Lambda_{v_i^h}$ from the 0th hop to $\hbar$th hop in lines 25–28.

Herein, it is worth mentioning that the source node may be unable to find an activated link set for the hth hop due to the lack of available nodes with sufficient residual energy. To address this issue, we employ a recursive approach to recover the candidate set from the void region and reselect the activated set, as shown in Algorithm 3. When determining the activated nodes of the hth hop given the activated nodes of the $(h+1)$th hop, if the source node fails to find an activated link set for the hth hop, it returns to the $(h+1)$th hop ($h+1 \neq 0$) and deletes the selected optimal set from all the candidate sets of the $(h+1)$th hop in lines 6–8. Using the updated $\mathbb{L}^{h+1}$ and $\mathbb{X}^{h+1}$, the algorithm recalculates the candidate nodes and links of the $(h+1)$th hop in line 8.

Algorithm 3 Void Recovery Mode

1: **function:** VoidRec( )
2: DATA: $\mathbb{X}^h$, $\mathbb{L}^h$
3: RESULT: updated $\mathbb{X}^h$, $\mathbb{L}^h$ and h
4: **if** $h < \hbar$ **then**
5: **while** $\mathbb{X}^h = \emptyset$ **do**
6: $h = h + 1$
7: delete element $(L_{z^*}^h)$ from $\mathbb{L}^h$ and element $(X_{z^*}^h)$ from $\mathbb{X}^h$
8: updated $\mathbb{L}^h$ and $\mathbb{X}^h$
9: **end while**
10: **end if**

D. Packet Forwarding

The source node employs Algorithms 1–3 to select the activated nodes and links. When the source needs to forward a packet pck_q to the destination, pck_q will be relayed between all selected activated nodes. The packet forwarding procedure is triggered when the source node's transmission queue contains at least one packet pck_q, as specified in Algorithm 4. The source node selects the activated links $\mathcal{L}_a$ and activated nodes $\mathcal{X}_a$ (determined by Algorithm 2) to deliver the packet pck_q in lines 3–7. The link selection procedure rehappens when the source node has sent D_u packets, i.e., when it starts a new epoch. After adding $\mathcal{L}_a$ and $\mathcal{X}_a$ to the header of packet pck_q, the source node de-queues the packet pck_q after timer Timer_TX expires (lines 9–11). Line 12 keeps track of the number of sent packets.

When the packet is being forwarded among the activated nodes, node v_i^h that receives the packet pck extracts the header information and stores it (line 15). If the link belongs to the activated link set, node v_i^h receives the entire packet and en-queues it; otherwise, it aborts the packet reception (lines 16–20). The lifetime of the network ends when the activated link set becomes null, i.e., the network can no longer execute the packet forwarding procedure. The number of sent packets q is defined as network longevity.

E. MAC

In the LRP, a collision avoidance MAC protocol with careful time scheduling is used at the MAC layer. Time-division multiplexing and advanced decoding technique (i.e., the Zigzag decoding technique [34]) are used, so the MAC

Algorithm 4 Packet Forwarding

$q = 0$
if pck_q in the source node's transmission queue **then**
  if a new epoch **then**
    $[\mathcal{X}_a, \mathcal{L}_a] =$ LinkSelec( )
  else
    $[\mathcal{X}_a, \mathcal{L}_a] =$ previous $[\mathcal{X}_a, \mathcal{L}_a]$
  end if
  add header information to pck_q
  while Timer_TX $= 0$ **do**
    $pck_q =$ de-queue packet
  end while
  $q = q + 1$
end if
if node v_i^h receives packet pck_q **then**
  extract packet header and store it
  if node $v_i^h \in \mathcal{X}_a$, $e_j^h \in \mathcal{L}_a$ and node v_i^h never has forwarded packet pck_q **then**
    receive packet and enqueue it
  else
    discard the packet
  end if
end if
if $\mathcal{L}_a = \emptyset$ **then**
  end the procedure
end if

protocol can support the proposed LRP routing protocol to avoid interference and maximize network throughput.

Given the lattice network topology of the UANs comprising sea-floor with acoustic transceivers, there are two categories of interference for the receiver: 1) the interference comes from the previous hop and 2) the interference comes from the rest of the nodes. For the first type of interference, the Zigzag decoding technique can decode collided packets by interference cancellation. For the second type of interference, using the time slot schedule can avoid collisions.

The time slot schedule is used to avoid the second type of interference. We assume that packet length pck_{size} is constant. Time is slotted and the duration of a time slot is t_{slot}, which is sufficient to transmit packets with the number of the maximum retransmissions. T time slots constitute a period. In each period, nodes in the same hop count will be assigned one slot to transmit. We define $l_p = \lceil \hbar/T \rceil$ the number of needed periods. In addition, the same slot will be reused by nodes $(wT - 1)$ hops away, where $w = 1, 2, \ldots, l_p$. Thus, nodes in $\mathcal{X}^h$ are assigned the $(h \bmod l_p)$th time slot in each period to transmit. Therefore, we can appropriately select T for collision-free communication given the lattice topology.

V. Parameter Analysis and Optimization

This section presents the parameter analysis and corresponding parameter optimization based on simulations. The ocean area is divided into $m \times n$ cubic regions in the simulation network setting, each with a length of D_s and an underwater sensor node. The network consists of 9–49 nodes, including a source node v_s and a destination node v_d. The objective is to establish multihop communication, where v_s transmits messages to v_d. We assume that each grid region forms a circle deployable range to allow deployment error where the node is deployed randomly. Thus, each node is randomly deployed in a circle at the center of each square with a radius of D_r ($D_r = [D_s/2]$). Accordingly, the maximum communication distance is $D_s + 2D_r$. We have adopted randomly generated network topologies. Upon completing the statistical analysis of one network's lifecycle, the next network topology is randomly generated, and subsequent simulations and statistical data collection are initiated. Each experiment records metrics, such as the total number of packets transmitted and ETE reliability until the network's energy is depleted.

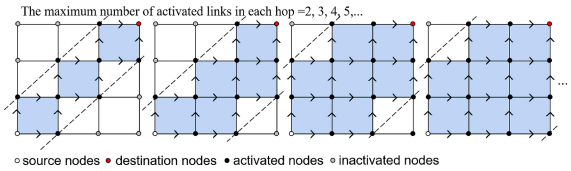

Fig. 3. Activated links with theoretical maximum ETE reliability for the homogeneous network.

After generating the topology, each node has specific properties, including attributes such as location, transmission range, and energy, among others. We have implemented the required routing protocols in Python, which encompass initialization procedures, link selection, and packet forwarding functionalities. In this section, we employed an approach of independent replication in our simulations. A set of experiments was repeated 500 times for each size of topology, where each experiment used the same initial conditions and parameter settings but introduced randomness through different random seeds.

A. Power Control Parameter

Power control is implemented by solving an optimization problem to reduce energy consumption while ensuring the success probability of a pair of nodes.

To determine the value of P_{req}, we employ a homogeneous network in this context, where the link success probability is equal for all links and is denoted as P_s. The activated links for the homogeneous network are depicted in Fig. 3, with variations in the maximum number of activated links (MNALs) for each hop. Here, we adopt a method for selecting activated nodes to achieve the maximum theoretical ETE reliability when the MNALs are restricted for each hop. Given the MNALs for each hop, higher ETE reliability can be achieved when the activated link is closer to the line connecting the source node to the destination node.

According to the ETE reliability calculation model, we can establish a relationship between the MNALs for each hop and the network's ETE reliability, considering a value of P_s. When $P_s = 0.85$, we analyze the maximum network ETE reliability while varying the MNALs for each hop from 2 to 7, as shown in Fig. 4(a). When the MNALs for each hop in the network are set to 2, the network's reliability decreases from

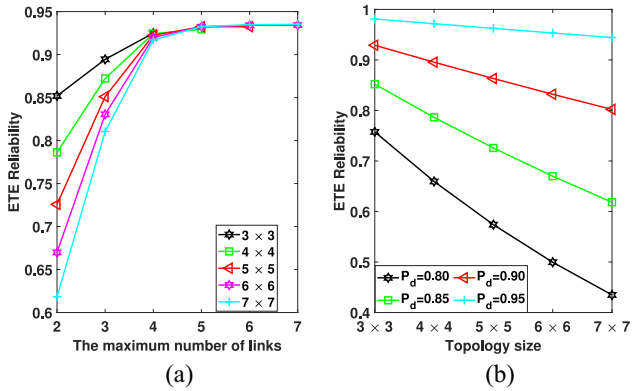

Fig. 4. ETE reliability for a homogeneous network (a) using different maximum activated links for each hop. (b) With different values of P_s when the MNALs for each hop equals two.

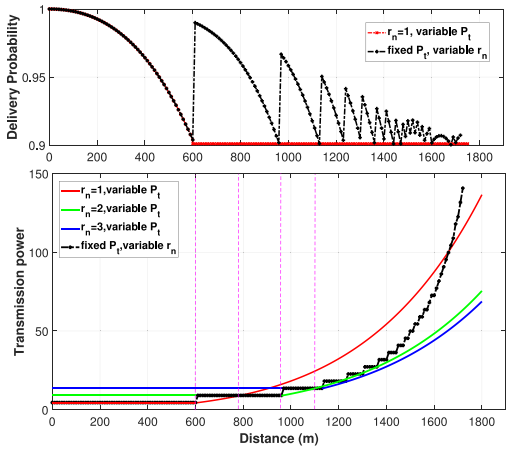

Fig. 5. Power control analysis.

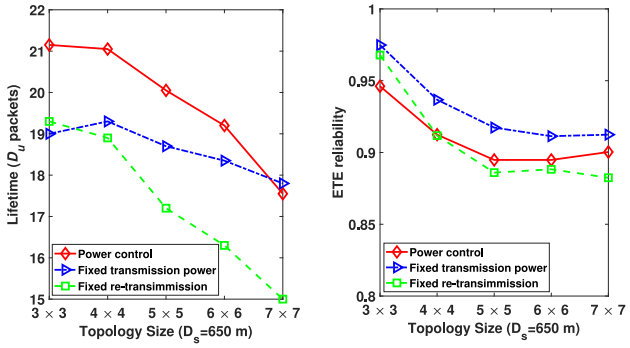

Fig. 6. Comparison of (a) average network longevity and (b) average ETE reliability under the implementation of power control.

0.85 to 0.62 as the network size increases. However, when the MNALs for each hop are set to 3, the reliability improves significantly, ranging from 0.9 to 0.8 for network sizes of 3×3 to 7×7. When the MNALs for each hop are set to 4, the network's reliability does not change much with the increase in network size, and all values exceed 0.9. Given the limited energy supply for UANs, we aim to use as few links as possible while meeting the reliability requirements. Therefore, we consider the case where the MNALs for each hop are two in the homogeneous network scenario. Following this, we conduct further analysis to determine the suitable value for P_{req} by examining the relationship between P_s and ETE reliability.

We calculate the impact of changes in P_s on network ETE reliability when the MNALs for each hop are set to 2. As the value of P_s decreases, the network reliability decreases more significantly. In Fig. 4(b), when $P_s = 0.8$, network reliability drops from approximately 0.75 in a 3×3 network to around 0.44 in a 7×7 network. When $P_s = 0.85$, network reliability is 0.61 for a 7×7 network. However, for $P_s = 0.9$, network reliability ranges from 0.91 to 0.8 as the network size increases from 3×3 to 7×7. When $P_s = 0.95$, network reliability consistently remains above 0.9.

Considering that the ETE reliability threshold Th is set above 0.85, when $P_s = 0.9$, and the MNALs for each hop are constrained to two, it becomes apparent that the theoretical maximum network ETE reliability ranges from 0.91 to 0.8. Within this context, there exists greater flexibility in selecting the states of network links to improve reliability and manage remaining energy. Therefore, we impose the constraint $P_{\text{req}} = 0.9$ as the required success probability for individual links. Node energy control is carried out based on this requirement, striking a reasonable balance between node transmission power and transmission times.

Fig. 5 illustrates how the retransmissions and variable p_t can affect the success probability and the total transmission power for a link. As the distance increases, the use of increased total transmission power improves the success probability of a pair of nodes. In the bottom part of Fig. 5, the black line represents the increased total transmission power with the increased retransmission. The corresponding success probability fluctuates between 0.9 and 1, as shown by the black line at the top, as each increase in the number of retransmissions leads to a spiked success probability. When the number of transmissions is fixed at 1, 2, and 3, corresponding to the red, green, and blue lines at the bottom, the total transmission power increases to maintain the success probability at 0.9 after a certain distance.

We calculate the power control problem mentioned in (9), and the results show that when the number of transmissions equals 1, the total transmission power increases significantly w.r.t. the distance. If a fixed transmission power is used, the number of transmissions increases quickly w.r.t. the distance to maintain the success probability. Therefore, we use a variable number of transmissions and variable transmission power for the link e_i^h with distance l_i^h, as given by

$$\begin{cases} p_t = p_0, r_n = 1, 0 \text{ m} < l_i^h \le 600 \text{ m} \\ P_s^{i,h}\left(l_i^h, p_t, 1\right) = 0.9, r_n = 1, 600 \text{ m} < l_i^h \le 780 \text{ m} \\ p_t = p_0, r_n = 2, 780 \text{ m} < l_i^h \le 970 \text{ m} \\ P_s^{i,h}\left(l_i^h, p_t, 2\right) = 0.9, r_n = 2, 970 \text{ m} < l_i^h \le 1080 \text{ m} \\ P_s^{i,h}\left(l_i^h, p_t, 3\right) = 0.9, r_n = 3, 1080 \text{ m} < l_i^h \le l_+ \text{ m} \end{cases} \tag{10}$$

where p_0 is the initial value of the transmission power, and l_+ is transmission range limitation.

To evaluate the performance of power control in LRP, we compare the network longevity and ETE reliability of three energy strategies with $\beta = 0.3$ and $Th = 0.90$, as depicted in Fig. 6(a) and (b). Our main objective is to maximize the

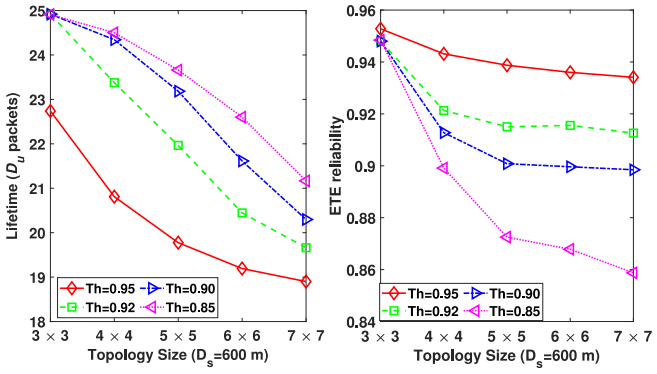

(a) (b)

Fig. 7. (a) Average lifetime and (b) average ETE reliability under different values of *Th*.

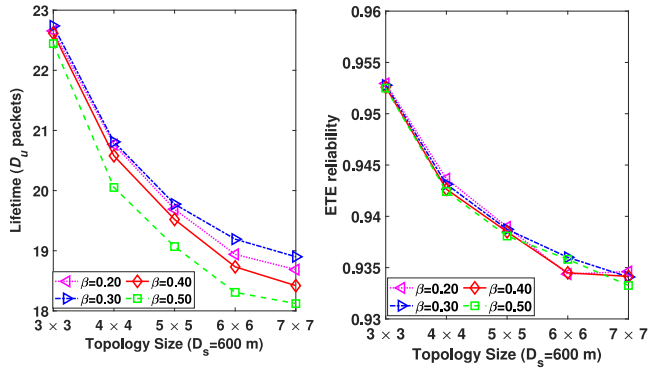

(a) (b)

Fig. 8. (a) Lifetime and (b) ETE reliability under different values of β.

network longevity of LRP with power control while ensuring ETE reliability. As the topology size increases, the network longevity decreases due to the larger network size, necessitating more links and energy consumption to maintain ETE reliability. It can be seen that LRP integrated with power control achieves the most prolonged network longevity while ensuring ETE reliability above the required threshold of 0.9. Furthermore, the decline in network longevity for the fixed transmission power strategy is comparatively lower than that of the other two strategies. That is attributed to the fact that the fixed transmission power corresponds to increased retransmission. The increased retransmission, denoted as *rn*, provides a certain level of redundancy in the success probability (as depicted in Fig. 5), resulting in fewer activated links for the fixed transmission power strategy than the other strategies.

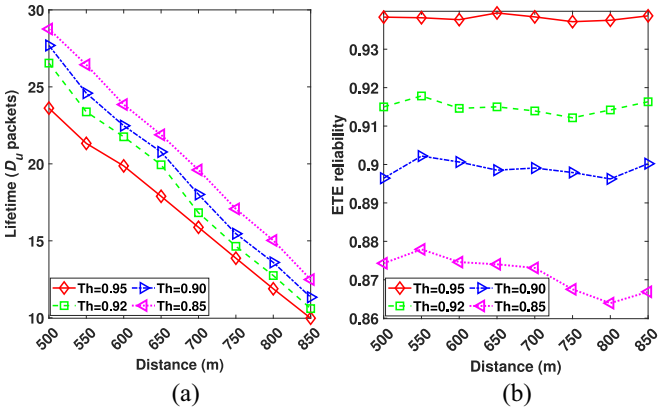

(a) (b)

Fig. 9. (a) Lifetime and (b) ETE reliability varying with distance under different values of *Th*.

B. Parameters Optimization

In this section, we assess the effect of the design parameters, including *Th*, β, and D_s, on the performance of network longevity and ETE reliability. Here, *Th* represents the required value of ETE reliability set by the source node, β is a coefficient in (8) that avoids the abuse of a specific node and balances the energy consumption of nodes at the same hop, and D_s denotes the length of the grid unit.

As shown in Fig. 7(a), when $\beta = 0.3$, the lifetimes under different *Th* values decrease as the network size increases. The per-hop reliability also rises with the increase in network size, given an ETE reliability threshold of *Th*. Higher per-hop reliability requirements lead to increased per-hop energy costs. Consequently, the network's lifetime shows a decreasing trend as the network size increases. Notably, the lifetimes corresponding to $Th = 0.95$ and $Th = 0.92$ exhibit a slower decline than those with $Th = 0.90$ and $Th = 0.85$. That is because an enormous value of *Th* results in a reduced impact on the per-hop reliability.

Given the ETE reliability tendency with different *Th* from Fig. 7(b), overall, LRP can satisfy the ETE reliability requirement and stabilize ETE reliability at around *Th*. It can be observed that the corresponding ETE reliability shows a decreasing trend as network size increases. Moreover, larger values of *Th* exhibit a shallower slope in the descent of ETE reliability, which is consistent with the behavior of exponential functions.

Fig. 8(a) and (b) illustrates the impact of different values of β on the network longevity and ETE reliability when $Th = 0.95$. It can be observed from Fig. 8(a) that the network achieves the most extended average lifetime when $\beta = 0.3$. Larger or smaller values of β are a source of disadvantage for network longevity. A lower value of β implies that the network consistently utilizes the same set of activated nodes until their energy is almost depleted, which reduces network longevity. Conversely, when the network adopts a larger value of β, the network longevity ends prematurely as a majority of nodes in the hth hop neighbors have an energy flag $\Lambda = 1$. As shown in Fig. 8(b), the corresponding ETE reliability remains unchanged because the reliability constraint is ensured during the routing selection procedure, and the network size is unchanged. The change of β can bring the change of $\mathcal{X}_a$ and $\mathcal{L}_a$, but the activated set still needs to satisfy the ETE reliability requirement.

We vary the side length of the grid from 500 to 850 m, and Fig. 9(a) and (b) presents the corresponding results in terms of network longevity and ETE reliability, with $\beta = 0.3$ and different values of *Th*. The network longevity decreases as the distance increases since the transmitting cost per hop increases, while the total original energy stored in each node

TABLE I
SETTING OF PARAMETERS

Parameter	Value
Spreading factor	2
D_u (packet)	1000
Th	0.95
β	0.3
Optimum carrier frequency	22.25 kHz
Absorption coefficient	4.5485 dB/km
Initial source level	177.3 dB
Reception directivity index	3
Working bandwidth	20 kHz
R_b	500 bps
p_r	0.5 w
p_0	4.5 w
pck_{size}	256 bits
Initial energy of sensors	80 kw ($G_\hbar$, $G_{\hbar-1}$, and G_1) 50 kw for others

remains unchanged. It should be noted that LRP still ensures ETE reliability within a range from Th to $Th - 0.01$ as the side length of the grid changes, as shown in Fig. 9(b). Nodes need to consume more energy to maintain the ETE reliability as the distance increases, leading to a reduced lifetime.

VI. PERFORMANCE EVALUATION

In this section, evaluation experiments based on the UAN model verify the performance of LRP regards overhead analysis, ETE reliability, network lifetime, and ETE delay. The simulation network setting is described in Section V. The specific parameters used in the simulations are presented in Table I. We employ a time-scheduling MAC protocol. At the source node, one packet is generated during each time slot. The time slot duration is $r_n \times ([pck_{\text{size}}/R_b] + [l_+/c] + \tau)$, where c represents the speed of sound, and τ denotes the guard interval. We set the maximal number of retransmissions as r_n. If a packet is retransmitted for r_n times without successful delivery, the node will simply discard this packet. In this section, we employ discrete event simulation to model packet transmission within the network.

A. Protocol Overhead

The overhead of LRP in exchanging data packets comes from two primary sources: 1) topology discovery and 2) the data packet headers. In UANs, topology information is crucial for executing MAC or routing protocols. Nodes may trigger initialization to obtain topology information after they are deployed undersea [30]. The control packet of topology discovery includes several fields, such as the *sender's ID*, *residual energy*, *transmission energy*, *location*, and *hops*. In a realistic network implementation, both the *ID* and *hop* of the node can each be represented by a 6-bit value, and a maximum of 64 sensor nodes are supported. A 16-bit value can represent the *residual energy*, *transmission power*, and *location*, respectively. The topology information of nodes needs to be collected no matter whether routing, MAC, or others use it. This part of the information is the basics of all routing protocols, so we assume LRP can directly use it. Moreover, the frequency of topology discovery can be adjusted to reduce this part of the overhead.

Furthermore, underwater communication has a larger packet header than terrestrial networks. However, LRP eliminates the need to transmit control packets frequently, and it just packets the routing information in the header of the data packets for a transmission at the beginning of the new period. The overhead of this field relies on the length of the path and the number of activated nodes, and it consists of the node's ID. In addition, the source node must compute a new routing path that can perform specific computations. The delay and power consumption introduced by computation is significantly lower than those of acoustic communications.

B. Protocol ETE Reliability and Longevity

We demonstrate the effectiveness of the proposed LRP by comparing it with several benchmarks named VBF [35], EEGNBR [24], GEDAR [9], and Multi-Shortest, respectively. Each of these routing techniques presents a distinct approach to underwater routing. In the VBF protocol, localization information is leveraged to establish a routing pipe with a radius of W extending from the sender to the destination node. Only nodes situated within this established routing pipeline are eligible to be selected as relays for forwarding messages. In this article, we set W as 500 m. EEGNBR provides underwater sensor nodes with the shortest route and adopts the forwarding protection mechanism to conserve energy consumption and prolong the network lifetime. GEDAR is a geographic and OR for UANs. Multi-Shortest is a multipath shortest protocol using the Dijkstra algorithm to find multiple shortest paths. We simulate the network longevity and the ETE reliability. We define D_u packets received by the destination as an epoch. Network longevity is defined as how many epochs the network runs before the source cannot select a path to the destination.

Fig. 10 illustrates the variation in network lifetime for different protocols across network topologies ranging from 3×3 to 7×7 in size. The results are calculated with a 95% confidence level, and the confidence intervals are represented by the green dashed lines. The box plots depict the distribution of network lifetime data for each protocol, including measures, such as median, interquartile range, maximum, minimum, and outliers.

We conducted an analysis of variance (ANOVA) test at a significance level of 0.05, which confirmed significant differences in network lifetimes between LRP and the other protocols. Compared to other routing protocols, LRP exhibits a higher median network lifetime, indicating its superior performance over the network lifetime. This superiority can be attributed to the energy control mechanisms within LRP, which effectively reduce energy consumption. By optimizing retransmission counts and transmission power, LRP minimizes energy usage. In contrast, GEDAR, VBF, and EEGNBR are single-path routing protocols. While they can select energy-efficient next-hop nodes, they often require high-power

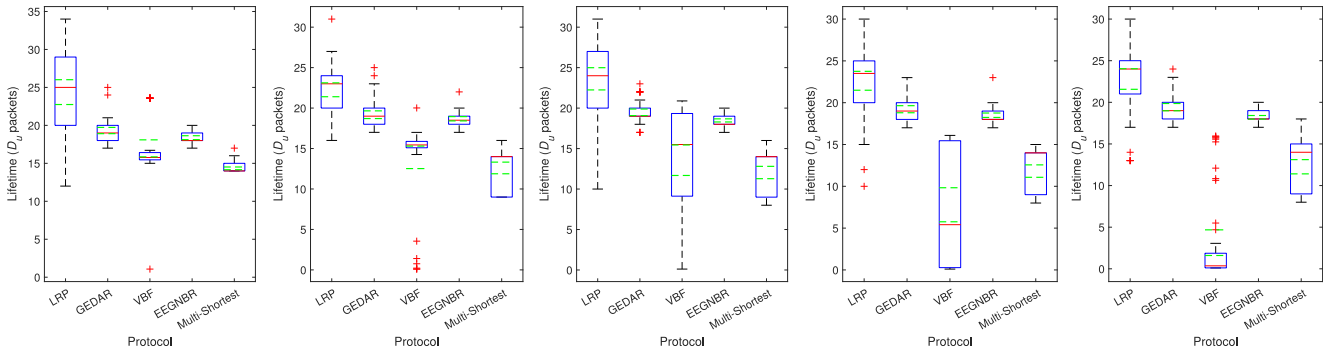

Fig. 10. Average network longevity is compared across various protocols within (a) 3×3, (b) 4×4, (c) 5×5, (d) 6×6, and (e) 7×7 network sizes.

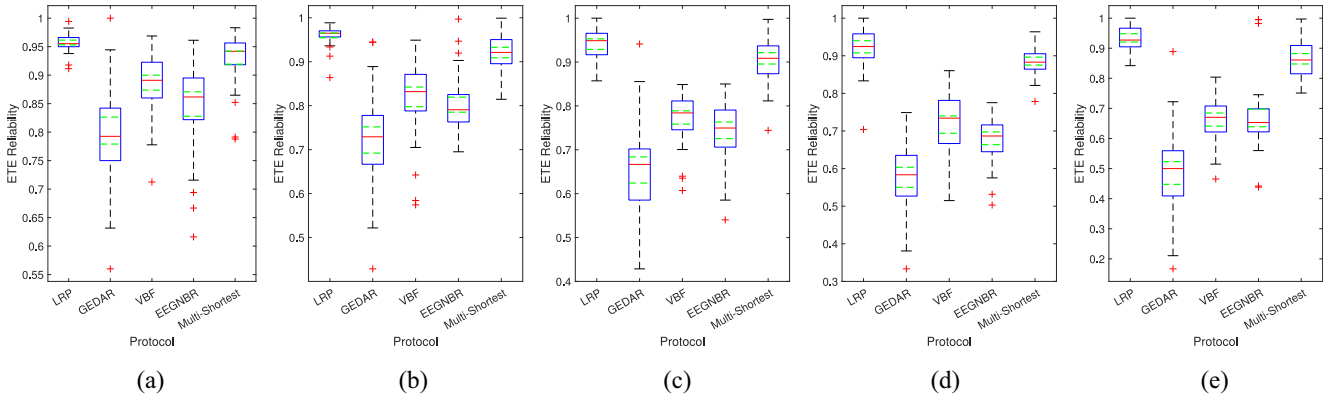

Fig. 11. Average network ETE reliability is compared across various protocols within (a) 3×3, (b) 4×4, (c) 5×5, (d) 6×6, and (e) 7×7 network sizes.

transmissions to achieve a certain delivery probability for each link.

LRP considers the residual energy of nodes to balance the selection of active nodes, which contribute to its extended network lifetime. However, GEDAR, VBF, and Multi-Shortest primarily consider node positions, which can lead to frequent use of nearby neighbors. Consequently, the imbalance in residual energy among nodes results in a decreased network lifetime. Notably, VBF exhibits the lowest network lifetime due to its inability to adaptively change the forwarding nodes within each round's forwarding cycle. It selects the forwarding node's one-hop neighbor within the routing pipe vector, leading to uneven energy consumption and susceptibility to the network topology and deployment methods. EEGNBR also considers the residual energy; however, when considering both residual energy and ETE reliability together, it exhibits worse lifetime performance than that of LRP.

Additionally, the network lifetime performance of LRP exhibits relative dispersion, which gradually diminishes with an increase in network size. This phenomenon is attributed to the relatively limited link selection space when the network size is small, which has some impact on node energy consumption. As the network size increases, the space for link selection expands, resulting in a more balanced energy consumption. The random deployment of the network leads to a wide span between maximum and minimum values in terms of network reliability. However, the network's lifetime can generally be maintained within the range of 20 000 to 25 000 packets. The simulated network lifetime exceeds that obtained from the theoretical parameter optimization section. This discrepancy arises because, in the theoretical parameter optimization section, link energy consumption is calculated based on the maximum number of transmissions. In contrast, in this section, link energy consumption is determined based on the actual number of transmissions.

Fig. 11 illustrates the variation in ETE reliability of different protocols across network topologies ranging from 3×3 to 7×7. The results are presented at a 95% confidence level, and the confidence intervals are depicted as green dashed lines. We conducted an ANOVA test with a significance level of 0.05, which confirmed the significant differences in ETE reliability values between LRP and the other protocols. The results show that the LRP protocol exhibits a higher median ETE reliability, a smaller interquartile range, and relatively fewer outliers. These findings indicate both higher and more stable network reliability with LPR. This superiority can be attributed to the energy control mechanisms within LRP, which effectively increase link success probabilities and the multipath percolation that explores multiple routes, ensuring ETE reliability. Multi-Shortest path closely follows, with an ETE reliability of approximately 0.9. This is because the Multi-Shortest path benefits from having multiple paths, each of which achieves a certain delivery probability. However, the lifespan of the Multi-Shortest path is significantly shorter than that of LRP,

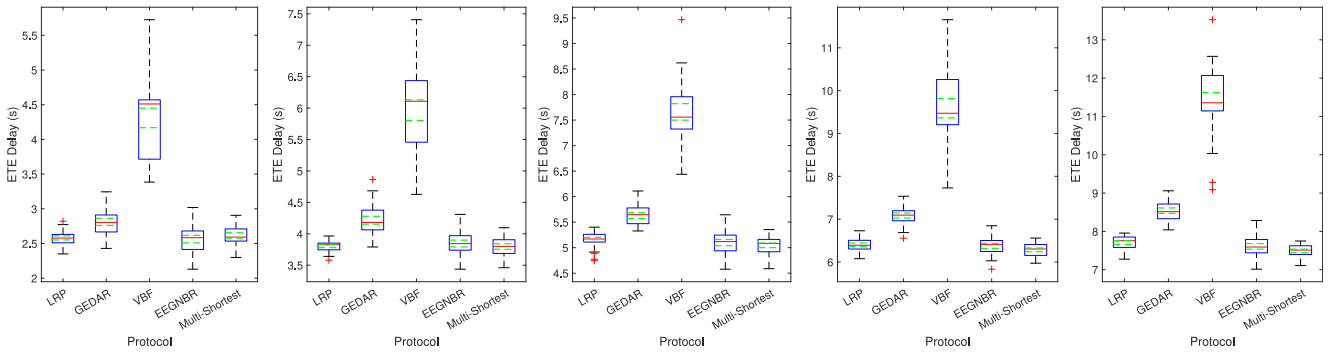

Fig. 12. Network average ETE delay is compared across various protocols within (a) 3 × 3, (b) 4 × 4, (c) 5 × 5, (d) 6 × 6, and (e) 7 × 7 network sizes.

primarily because it considers only distance and does not account for the ETE reliability offered by the selected path.

The ETE reliability displayed by VBF, GEDAR, and EEGNBR is lower than that of LRP, and their ETE reliability decreases noticeably with increasing network size. This decline in ETE reliability can be attributed to diminishing gains in link success probabilities for ETE reliability as the network size grows. Additionally, VBF, GEDAR, and EEGNBR have lower per-hop reliability when compared to LRP. These factors collectively contribute to LRP achieving superior ETE reliability.

With the increase in network size, the distribution of ETE reliability for other protocols becomes relatively dispersed, and a significant decrease is observed in their reliability. In contrast, LRP maintains an ETE reliability between 0.9 and 0.98 across various network sizes. This is achieved by dynamic link selection and an increased number of activated links per hop, ensuring that LRP consistently maintains high and stable ETE reliability.

We acknowledge that the underlying MAC protocol can significantly impact the ETE delay. Therefore, when all five protocols employ the same MAC protocol discussed in Section IV-E, they exhibit similar ETE delays, assuming they have the same hop count (except for VBF). To compare the path selection superiority of each protocol using ETE delay results, we aim to eliminate the influence of the underlying protocols on ETE delay by disregarding the delay caused by MAC.

Fig. 12 presents the average ETE delay at a 95% confidence level, demonstrating that LRP, GEDAR, EEGNBR, and Multi-Shortest exhibit similar ETE delay. Furthermore, it is evident that VBF exhibits the highest ETE delay. VBF tends to select the node closest to the routing vector, resulting in a relay node potentially being located far away from the sender, leading to a longer propagation delay.

VII. Conclusion

This article proposed a novel routing protocol, LRP, explicitly designed for underwater sensor networks to prolong network longevity and ensure ETE reliability. The building of hop-count-based graph and the effective configuration of transmission power and retransmission can be completed during initialization. LRP can select activated links and nodes for message forwarding using nodes' residual energy and the estimated reliability hop by hop. During the source routing selection and message percolation forwarding procedure, LRP does not need to use more exchange of control messages. As a result, LRP surpasses other protocols regarding ETE reliability, network longevity, and ETE delay. Through extensive simulations, we demonstrated that LRP outperforms existing state-of-the-art routing protocols, such as VBF, GEDAR, EEGNBR, and Multi-Shortest.

In our future work, we will optimize the protocol to improve its performance, specifically by exploring a combined MAC layer and LRP design. We acknowledge that the current use of a recursion algorithm in LRP may limit its suitability for large-scale networks, and we plan to address this challenge in our further research. Furthermore, we are particularly interested in investigating percolation routing techniques that aim to minimize the Age of Information (AoI). That will involve associating transmission schedule designs that enable multiple simultaneous transmissions, ultimately enhancing the timeliness of information delivery in the network.

References

[1] T. Qiu, Z. Zhao, T. Zhang, C. Chen, and C. L. P. Chen, "Underwater Internet of Things in smart ocean: System architecture and open issues," *IEEE Trans. Ind. Informat.*, vol. 16, no. 7, pp. 4297–4307, Jul. 2020.

[2] E. M. Sozer, M. Stojanovic, and J. G. Proakis, "Underwater acoustic networks," *IEEE J. Ocean. Eng.*, vol. 25, no. 1, pp. 72–83, Jan. 2000.

[3] L. Freitag, M. Johnson, and D. Frye, "High-rate acoustic communications for ocean observatories-performance testing over a 3000 m vertical path," in *Proc. MTS/IEEE Conf. Exhibit. Conf.*, vol. 2, 2000, pp. 1443–1448.

[4] M. Stojanovic and P.-P. J. Beaujean, "Acoustic communication," in *Springer Handbook of Ocean Engineering*. Cham, Switzerland: Springer, 2016, pp. 359–386.

[5] V. Raina and M. K. Jha, "QoS evaluation of square-grid topology in underwater acoustic sensor networks," in *Proc. 1st Int. Conf. Next Gener. Comput. Technol. (NGCT)*, 2015, pp. 269–273.

[6] S. Lmai, M. Chitre, C. Laot, and S. Houcke, "Throughput-maximizing transmission schedules for underwater acoustic multihop grid networks," *IEEE J. Ocean. Eng.*, vol. 40, no. 4, pp. 853–863, Oct. 2015.

[7] S. Wang, Y. Wang, and X. Guan, "An interference-free scheduling for the TDMA protocol in multi-hop underwater acoustic grid networks," in *Proc. OCEANS*, 2017, pp. 1–5.

[8] J. Heidemann, M. Stojanovic, and M. Zorzi, "Underwater sensor networks: Applications, advances and challenges," *Philos. Trans. Royal Soc. A, Math., Phys. Eng. Sci.*, vol. 370, no. 1958, pp. 158–175, 2012.

[9] R. W. L. Coutinho, A. Boukerche, L. F. M. Vieira, and A. A. F. Loureiro, "Geographic and opportunistic routing for underwater sensor networks," *IEEE Trans. Comput.*, vol. 65, no. 2, pp. 548–561, Feb. 2016.

[10] Y. Noh et al., "HydroCast: Pressure routing for underwater sensor networks," *IEEE Trans. Veh. Technol.*, vol. 65, no. 1, pp. 333–347, Jan. 2016.

[11] Y. Noh, U. Lee, P. Wang, B. S. C. Choi, and M. Gerla, "VAPR: Void-aware pressure routing for underwater sensor networks," *IEEE Trans. Mobile Comput.*, vol. 12, no. 5, pp. 895–908, May 2013.

[12] Q. Wang, J. Li, Q. Qi, P. Zhou, and D. O. Wu, "An adaptive-location-based routing protocol for 3-D underwater acoustic sensor networks," *IEEE Internet Things J.*, vol. 8, no. 8, pp. 6853–6864, Apr. 2021.

[13] Q. Guan, F. Ji, Y. Liu, H. Yu, and W. Chen, "Distance-vector-based opportunistic routing for underwater acoustic sensor networks," *IEEE Internet Things J.*, vol. 6, no. 2, pp. 3831–3839, Apr. 2019.

[14] R. W. L. Coutinho and A. Boukerche, "OMUS: Efficient opportunistic routing in multi-modal underwater sensor networks," *IEEE Trans. Wireless Commun.*, vol. 20, no. 9, pp. 5642–5655, Sep. 2021.

[15] Y. Zhang, Z. Zhang, L. Chen, and X. Wang, "Reinforcement learning-based opportunistic routing protocol for underwater acoustic sensor networks," *IEEE Trans. Veh. Technol.*, vol. 70, no. 3, pp. 2756–2770, Mar. 2021.

[16] J. Luo, Y. Chen, M. Wu, and Y. Yang, "A survey of routing protocols for underwater wireless sensor networks," *IEEE Commun. Surveys Tuts.*, vol. 23, no. 1, pp. 137–160, 1st Quart., 2021.

[17] S. Khisa and S. Moh, "Survey on recent advancements in energy-efficient routing protocols for underwater wireless sensor networks," *IEEE Access*, vol. 9, pp. 55045–55062, 2021.

[18] C.-J. Huang, Y.-W. Wang, H.-H. Liao, C.-F. Lin, K.-W. Hu, and T.-Y. Chang, "A power-efficient routing protocol for underwater wireless sensor networks," *Appl. Soft Comput.*, vol. 11, no. 2, pp. 2348–2355, 2011.

[19] T. Hu and Y. Fei, "QELAR: A machine-learning-based adaptive routing protocol for energy-efficient and lifetime-extended underwater sensor networks," *IEEE Trans. Mobile Comput.*, vol. 9, no. 6, pp. 796–809, Jun. 2010.

[20] U. Draz et al., "Energy efficient proactive routing scheme for enabling reliable communication in underwater Internet of Things," *IEEE Trans. Netw. Sci. Eng.*, vol. 8, no. 4, pp. 2934–2945, Oct.–Dec. 2021.

[21] R. Ruby, S. Zhong, B. M. ElHalawany, H. Luo, and K. Wu, "SDN-enabled energy-aware routing in underwater multi-modal communication networks," *IEEE/ACM Trans. Netw.*, vol. 29, no. 3, pp. 965–978, Jun. 2021.

[22] Y. Zhou, T. Cao, and W. Xiang, "Anypath routing protocol design via Q-learning for underwater sensor networks," *IEEE Internet Things J.*, vol. 8, no. 10, pp. 8173–8190, May 2021.

[23] Y. Sun, M. Zheng, X. Han, S. Li, and J. Yin, "Adaptive clustering routing protocol for underwater sensor networks," *Ad Hoc Netw.*, vol. 136, Nov. 2022, Art. no. 102953.

[24] Z. Liu, X. Jin, Y. Yang, K. Ma, and X. Guan, "Energy-efficient guiding-network-based routing for underwater wireless sensor networks," *IEEE Internet Things J.*, vol. 9, no. 21, pp. 21702–21711, Nov. 2022.

[25] B. Bollobás and O. Riordan, *Percolation*. Cambridge, U.K.: Cambridge Univ. Press, 2006.

[26] v. M. Sahini and M. Sahimi, *Applications of Percolation Theory*. Boca Raton, FL, USA: CRC Press, 1994.

[27] Y. Liu, L. Cai, J. Hu, X. Shen, and H. Wang, "LRP: Long-lifetime and reliable percolation routing for underwater sensor networks," in *Proc. IEEE 23rd Int. Conf. High Perform. Switch. Rout. (HPSR)*, 2022, pp. 29–34.

[28] J. Hu, L. Cai, and J. Pan, "Mesh network reliability analysis for ultra-reliable low-latency services," in *Proc. IEEE 18th Int. Conf. Mobile Ad Hoc Smart Syst. (MASS)*, 2021, pp. 198–206.

[29] J. Hu, L. Cai, C. Zhao, and J. Pan, "Directed percolation routing for ultra-reliable and low-latency services in low earth orbit (LEO) satellite networks," in *Proc. IEEE 92nd Veh. Technol. Conf. (VTC-Fall)*, 2020, pp. 1–6.

[30] Y. Liu, H. Wang, L. Cai, X. Shen, and R. Zhao, "Fundamentals and advancements of topology discovery in underwater acoustic sensor networks: A review," *IEEE Sensors J.*, vol. 21, no. 19, pp. 21159–21174, Oct. 2021.

[31] J. Liu, Z. Wang, M. Zuba, Z. Peng, J.-H. Cui, and S. Zhou, "DA-Sync: A doppler-assisted time-synchronization scheme for mobile underwater sensor networks," *IEEE Trans. Mobile Comput.*, vol. 13, no. 3, pp. 582–595, Mar. 2014.

[32] O. Pallares, P.-J. Bouvet, and J. del Rio, "TS-MUWSN: Time synchronization for mobile underwater sensor networks," *IEEE J. Ocean. Eng.*, vol. 41, no. 4, pp. 763–775, Oct. 2016.

[33] G. Liu, S. Yan, and L. Mao, "Receiver-only-based time synchronization under exponential delays in underwater wireless sensor networks," *IEEE Internet Things J.*, vol. 7, no. 10, pp. 9995–10009, Oct. 2020.

[34] S. Gollakota and D. Katabi, "Zigzag decoding: Combating hidden terminals in wireless networks," in *Proc. ACM SIGCOMM Conf. Data Commun.*, 2008, pp. 159–170.

[35] P. Xie, J.-H. Cui, and L. Lao, "VBF: Vector-based forwarding protocol for underwater sensor networks," in *Proc. Int. Conf. Res. Netw.*, 2006, pp. 1216–1221.

Yuan Liu (Member, IEEE) received the M.S. degree in electrical engineering from the School of Marine Science and Technology, Northwestern Polytechnical University, Xi'an, China, in 2019, where she is currently pursuing the Ph.D. degree with a focus on underwater acoustic networks.

She was a visiting Ph.D. student with the Department of Electrical and Computer Engineering, University of Victoria, Victoria, BC, Canada. Her research interests include underwater network and communications, protocols design in underwater wireless networks, and topology inference.

Haiyan Wang received the B.S., M.S., and Ph.D. degrees in electrical engineering from the School of Marine Science and Technology, Northwestern Polytechnical University (NPU), Xi'an, China, in 1987, 1990, and 2004, respectively.

He has been a Faculty Member since 1990 and a Professor since 2004 with NPU. He has been a Professor with the School of Electronic Information and Artificial Intelligence, Shaanxi University of Science and Technology, Xi'an, since 2018. He teaches and conducts research in signal and information processing, electronic engineering, and tracking and locating maneuvering targets with NPU. His general research interests include modern signal processing, array signal processing, voice signal processing, artificial intelligence, machine learning, underwater acoustic communications, tracking and locating of maneuvering targets, and data mining techniques and their application.

Lin Cai (Fellow, IEEE) received the M.A.Sc. and Ph.D. degrees (awarded Outstanding Achievement in Graduate Studies) in electrical and computer engineering from the University of Waterloo, Waterloo, ON, Canada, in 2002 and 2005, respectively.

Since 2005, she has been with the Department of Electrical and Computer Engineering, University of Victoria, Victoria, BC, Canada, where she is currently a Professor. Her research interests span several areas in communications and networking, with a focus on network protocol and architecture design supporting emerging multimedia traffic and the Internet of Things.

Prof. Cai is an NSERC E.W.R. Steacie Memorial Fellow, an Engineering Institute of Canada Fellow, and a Canadian Academy of Engineering Fellow. In 2020, she was elected as a Member of the Royal Society of Canada's College of New Scholars, Artists and Scientists, and a 2020 "Star in Computer Networking and Communications" by N2Women.

Junhao Hu received the B.S. degree in computer science and technology from Northwest University, Xi'an, China, in 2016, and the M.A.Sc. degree in electrical and computer engineering from the University of Victoria, Victoria, BC, Canada, in 2021.

His research focuses on the calculation of directed connectivity, ultrareliable and low-latency networks, and routing for low-Earth orbit.

Xiaohong Shen (Member, IEEE) received the B.S., M.S., and Ph.D. degrees in electrical engineering from the School of Marine Science and Technology, Northwestern Polytechnical University, Xi'an, China, in 1987, 1998, and 2008, respectively.

Since 2016, she has been the Vice-Director of the Key Laboratory of Ocean Acoustics and Sensing, Ministry of Industry and Information Technology, Beijing, China. She is currently a Professor with the School of Marine Science and Technology, Northwestern Polytechnical University. She is the Principal Investigator of grants supported by the National Natural Science Foundation of China. Her general research interests include underwater acoustic signal processing and communications.